Modelling and Simulation in Materials Science and Engineering

PAPER

Molecular insights into shock responses of amorphous polyethylene

To cite this article: Lijuan Liao *et al* 2021 *Modelling Simul. Mater. Sci. Eng.* **29** 015008

IOP Publishing Modelling and Simulation in Materials Science and Engineering
Modelling Simul. Mater. Sci. Eng. **29** (2021) 015008 (18pp) https://doi.org/10.1088/1361-651X/abcd89

Molecular insights into shock responses of amorphous polyethylene

Lijuan Liao[1,*], Xintianyang Wang[1,2] and Chenguang Huang[1,2,3,4]

[1] Key Laboratory for Mechanics in Fluid Solid Coupling Systems, Institute of Mechanics, Chinese Academy of Sciences, No. 15, Beisihuan West Road, Haidian District, Beijing 100190, People's Republic of China
[2] School of Future Technology, University of Chinese Academy of Sciences, No. 19(A), Yuquan Road, Shijingshan District, Beijing 100049, People's Republic of China
[3] School of Engineering Science, University of Chinese Academy of Sciences, No. 19(A), Yuquan Road, Shijingshan District, Beijing 100049, People's Republic of China
[4] Hefei Institutes of Physical Science, Chinese Academy of Sciences, No. 350, Shushanhu Road, Hefei, Anhui 230031, People's Republic of China

E-mail: liaohuanxin@hotmail.com

Received 3 August 2020, revised 7 November 2020
Accepted for publication 24 November 2020
Published 10 December 2020

Abstract

Shock responses of amorphous polyethylene (APE) were characterized utilizing two different types of methodology, direct non-equilibrium molecular dynamics (NEMD) and multi-scale shock technique (MSST). Providing a detailed physical view of the shock front itself, pico-second time resolved evolution of plasticity behind the shock front was explored by NEMD through simulating piston driven shock compression. The induced-shock propagation and reflection were visualized according to the evolution of the particle displacement, particle velocity field and pressure field. Exponential relations between the compression rate in a shock wave and the hydrodynamic pressure, in addition, the thickness of shock front and the hydrodynamic pressure were clarified, which quantitatively indicate the shrinkage of shock front resulted from higher compression strength under larger piston velocity. On the other hand, in addition to reproducing the final compressed states, the thermo-dynamical state variables behind the leading shock front were captured by MSST with a much smaller computational cell with enough efficiency and accuracy. Hugoniot relations were obtained to predict the bulk sound speed and two material

*Author to whom any correspondence should be addressed.

constants indicating the compressibility with reliable values compared with the existing results. Temperature-dependency was clarified as that high temperature reduces the bulk sound speed with low density and improves the compressibility of material. The temperature-sensitivity of compressibility weakens or even disappears during the transition from glassy state to rubbery state. The critical shock velocity, which equals to the bulk sound speed at a given temperature, was specified to guarantee stable shock wave instead of quasi-isentropic wave propagation in APE. Only a single plastic shock wave with a steep front travelling at a constant velocity greater than the bulk sound speed generates in APE, resulting in the over-driven in the material.

Keywords: shock responses, amorphous polyethylene, molecular insight, wave propagation, shock Hugoniot

(Some figures may appear in colour only in the online journal)

1. Introduction

Polymers are widely adopted such as in adhesive or coating to connect components, bear and transmit loadings [1]. Unavoidably, structures and materials experience sudden high pressure in practical applications, for example, commonly found in aeronautical, mechanical, ocean, and transportation engineering fields. The complex characteristics of polymers in extreme conditions are vital to estimate the mechanical performances of the whole system involving polymers.

A significant interest in the shock wave propagation behavior of polymer fibers has been devoted. Especially, the mechanical responses behind the shock front are significant characteristics of the material, which are the objects in optimization and regulation for improving the performances of the system. With the development of atomic response measurements at spatiotemporal scales well matched with computational molecular dynamics (MD), e.g. laser-induced shock waves and femtosecond time-resolved optical diagnostics, new opportunities for direct collaboration between experiment and simulation arise currently [2]. Compared with kinetic performances, the transformation of molecular structures of polymers under shock loadings is more difficult to be obtained via experiments [3]. Taking the distinct length scales at continuum (i.e. macro) and particle (i.e. micro/atomistic) into account, bridging physical quantities between scales has been implemented by extending the original Hardy's methodology and modifying Admal & Tadmor's formulas to generate heat flux expressions aiming to polyethylene [4].

Taking the complex chain or crosslink structures of polymers into account, bottom approach at atomic or molecular scales is an ideal option to clarify the mechanical mechanism and provide design guidelines of polymers with better performances [5]. Accordingly, the details of evolution of particle velocities induced by an extremely rapid impact in the specified system should be described primarily. MD modeling on impact dynamics generally falls into two categories according to explicit or implicit shock wave.

One representative explicit approach is modeling a virtual piston or flyer plate to generate shock waves [3, 6–11], which is a typical non-equilibrium molecular dynamics (NEMD) method. The details of wave propagation and reflection can be captured by studying the local, dynamic effects. Correspondingly, the spatiotemporal evolution of the pressure, temperature and energy yielded by the shock provide valuable information to understand the dynamic

responses of the system. Accordingly, the modification of polymers and polymer-based composites for performance improvement is feasible with more clear physical insight. In the work carried out by Fu *et al* [10], the enhancement of energy absorption of polyethylene polymer modified by nanocomposites was reported on the dynamics responses to shock wave loading.

Opposite to explicit shock wave, equilibrium methods focus on the thermodynamic state behind the shock front rather than the dynamic shock event itself. Combining atomistic simulations with the Euler equations for compressible flow, multi-scale shock technique (MSST) proposed by Reed *et al* [12] follows a Lagrangian point through the shock wave with significantly fewer atoms and lower computational cost. This is akin to switching from an Eulerian to a Lagrangian frame [13]. Shock Hugoniot and Mie-Grüneisen equation of state (EOS) of alloy [14], shock induced deformation response [15] and metastable phase of single crystal copper [16], shock compression of polyvinyl chloride [17], shock-induced phase transition of water [18], orientation dependence of shock-induced initiation of explosives [19], thermodynamic states throughout the reaction zone of explosives [20], steady shock waves in materials [21], *et al* have been examined by MSST with reliable results, providing new findings in microstructure evolution. Among them some works were validated by comparing with the results obtained by NEMD.

In this study, polyethylene (PE), as a linear polymer with repeat methylene monomers, was chosen as the representative polymer for simplicity. Taking NEMD and MSST advantages into account in a balanced manner, both methods were adopted to examine the shock responses of PE. Particular attention was put on the dynamics wave propagation and the thermodynamic state behind a shock front simultaneously. The main goal of this study is to establish effective and usable data visualization and characterization methods that are capable of clarifying the details of the typical polymer responses subjected to dynamic compression and grasping the key characteristics. This will be helpful to determine the controlling parameters and provide design guidelines for further and deeper research.

The article is organized as follows. In section 2, the computational details are introduced, including the model building and the settings for calculations. In section 3, the dynamic wave propagations and the Hugoniot behaviors are described. We also discuss the evolutions of the thermodynamics parameters and the stability of the dynamic wave. In addition, related discussion is carried out. Finally, the conclusions are summarized.

2. Details of computational models

With repeat methylene monomers-$[-CH_2-]_n-$ ($n = 200$, indicates the chain length) along the backbone in a single PE chain, molecular models with united atoms (UA) were built to save computational expensive (displayed as the upper part of figure 1). As a typical coarse-grained approach [22, 23], each UA represents one methylene group [5, 24]. Each system was modeled with a relatively low density initially by throwing PE chains randomly into a box via Packmol [25], as shown in figures 1(a) and (c). The Dreiding potential [24] is used to determine the interactions between UA. Corresponding parameters are referred to those described in our previous work [5]. Time step was 1 fs during relaxation.

Rather than a cubic box model with all-periodic boundary condition (BC) in MSST computational scheme (as shown in figures 1(c) and (d)), a relatively long box in the impact direction ($\sim$1000 Å in the z-direction) was modeled for NEMD calculations to observe the progression of the dynamic wave clearly before it reflected from the opposite edge of the PE bar (as shown in figure 1(a)). Open-end of the bar was connected with a reflective wall (i.e. infinite impedance) or a region of vacuum (i.e. zero impedance), which was chosen by designing the reflective

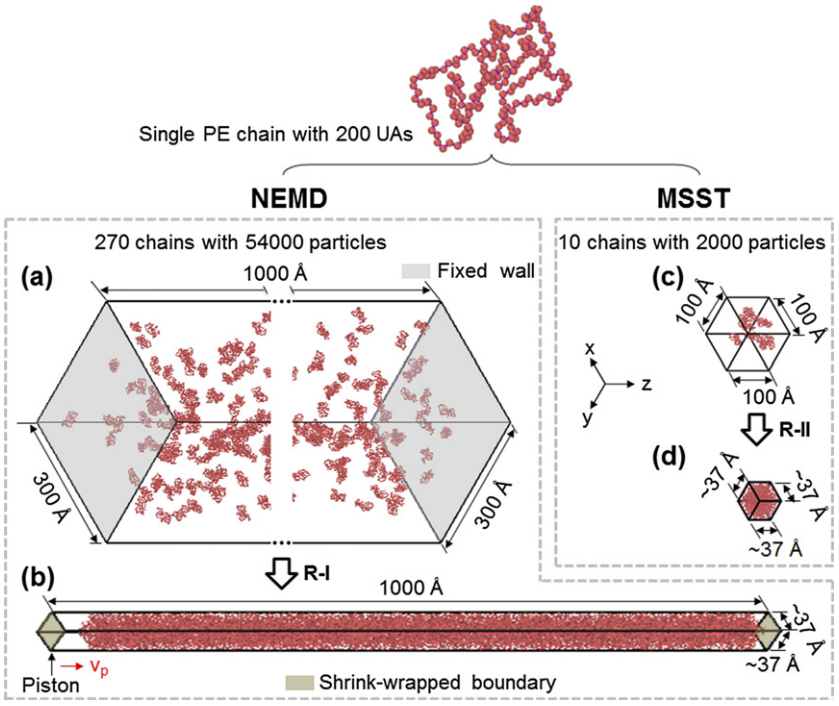

Figure 1. Examples of MD models at initial state for (a) NEMD and (c) MSST calculations, and at equilibrium at 100 K by (b) NEMD and (d) MSST methods.

condition or not during simulation as needed. Periodic BC was imposed in the cross-sectional directions (x- and y-directions), which mimics the response of PE away from the lateral free surfaces.

Each relaxation process for NEMD (denoted as R-I) or MSST (denoted as R-II) computational schemes was illustrated in figure 2, where T, P and t_{relax} are the temperature, pressure and relaxation duration at each ensemble. T_0 is the target temperature for each system at initial un-shocked reference state. It should be pointed out that sufficient relaxation should be run for temperatures well above the glass transition (denoted as T_g) [26]. T_g was calculated as around 250 K previously [5], and it ranges from 190 to 300 K in experiments [27] for PE system. The high temperature 500 K above T_g at the beginning of relaxation was set to eliminate the overlap of chains and promote them to satisfy Brownian motion. In addition, we paid more attention to the shock responses of the systems at the glassy state below T_g. Especially for NEMD computational scheme with much larger system compared with MSST simulation, computing cost is one of important factors to consider. Two cooling rates (denoted as r_c) 0.05 and 0.5 K ps^{-1} from 500 to 100 K were examined to determine the annealing duration. In addition, the effect of t_{relax} (500 ps and 1 ns) at the last step in R-I (denoted as $t_{\text{relax-end}}$) was discussed. The sensitivities of r_c and $t_{\text{relax-end}}$ on the mean square internal distances $\langle R^2 \rangle$ ($|i - j|$, N) [26] were examined. The values of $\langle R^2 \rangle$ are 920.6 Å^2 (r_c = 0.5 K ps^{-1}, $t_{\text{relax-end}}$ = 500 ps), 918.1 Å^2 (r_c = 0.05 K ps^{-1}, $t_{\text{relax-end}}$ = 500 ps) and 919.1 Å^2 (r_c = 0.05 K ps^{-1}, $t_{\text{relax-end}}$ = 1 ns), respectively, as an example from one sample running in each case. Taking account of the computational efficiency and accuracy simultaneously, r_c = 0.5 K ps^{-1} and $t_{\text{relax-end}}$ = 500 ps, which are listed in figure 2(a), were adopted in NEMD simulations. The

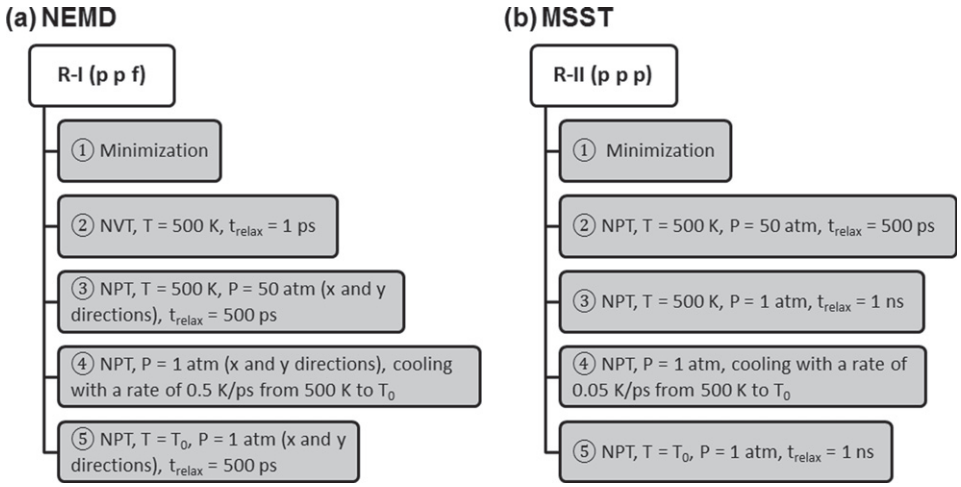

Figure 2. Flowcharts of relaxation process for (a) NEMD and (b) MSST computational schemes.

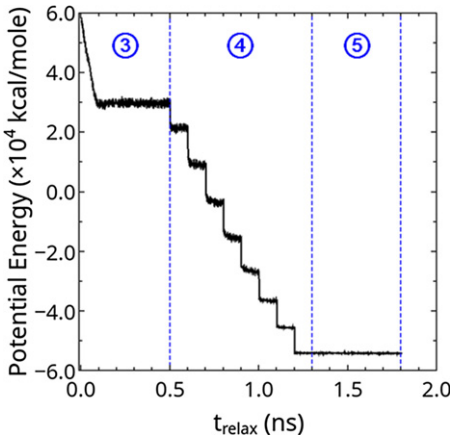

Figure 3. Variation of potential energy during the last three steps of the relaxation for NEMD computed scheme as an example.

variation of potential energy of 1 PE bar system for NEMD computational scheme according to R-I as an example was monitored as shown in figure 3. We assumed that the relaxation procedure is acceptable to reach the equilibrium.

From the point view of statistics, 6 separate simulation runs with different random velocity seeds were carried out for each case discussed in the present study. All MD runs and visualizations were implemented by LAMMPS [28] and OVITO [29], respectively. Each value of the local p_2 order parameter [30, 31] for all the configurations at equilibrium was near zero, which supports that all the established models are amorphous polyethylene (APE) boxes here.

Taking $T_0 = 100$ K at equilibrium as an example (APE at glassy state), the sizes in the cross-sectional directions (x- and y-directions) for NEMD calculations (as shown in figure 1(b)) are

close to those of the model prepared for MSST runs (as shown in figure 1(d)). This helps to compare the results obtained by the two methods with the same magnitude of cross-sectional area across the dynamics waves.

Adopting NEMD, a dynamic wave was generated by moving a rigid wall toward the APE bar along the z-direction at a constant velocity v_p for a given duration, which mimics an impact with an infinite-impedance flyer plate moving at a velocity v_p (as shown in figure 1(b)). Adiabatic MD simulations were carried out to describe the dynamical evolution of the bar cell. On the other hand, the responses of the APE cell were examined behind a shock front with a shock speed v_s by MSST, which is a kind of Lagrangian method. It is clear to find the large difference on the computational efficiency between the two ways owing to the differences of the sizes of the calculation cells and number of particles. A quadratic speedup [12, 32] or even of 10^9 over the direct shock-simulation approach was reported [33], which means that a longer simulation is possible with higher efficiency by MSST.

3. Results and discussion

3.1. Wave propagation and reflection

Taking piston velocity $v_p = 5.0$ km s^{-1} at $T_0 = 100$ K as an example, the snapshots for the temporal evolutions of particle displacements along the compression direction (z-direction) in APE bars were illustrated in figure 4 with a free open-end (figure 4(a)) and a reflective wall (figure 4(b)). Under the piston compression, APE UAs were driven forward at the same velocity v_p successively. The compression-induced shock wave propagates into the material with v_s ($>v_p$) from left to right until the open-end of the bar. The material at the upstream of the shock wave is compressed and that at the downstream remains at rest.

As illustrated in figures 5(a) and (b), the spatiotemporal evolution of pressure (virial stress denoted as P_{zz} paralleled to the shock direction) indicates a clear line of demarcation between the shocked- and the initial-state of the APE bar. A steady propagation of the shock wave with a constant velocity in the APE bar until it reaches the open-end was observed both with different BCs. Owing to the same wave propagation velocity v_s until reaching the open-end at t_e (marked on the time axis as red diagonal cross '$\times$' in figures 5(a) and (b)), v_s–v_p relation is independent of BC. On the other hand, BC controls the reflection of the shock wave. For the BC of free open-end connected with a region of vacuum in figure 4(a), the particles at the open-end are travelling at twice of v_p forward driven by the shock front as illustrated in figure 5(a). This corresponds with the fact that when a compressive wave arrives to a free surface with zero impedance, the particle velocity is doubled. Following a high pressure region swept by the compression wave front, a release fan generates resulting from the reflective tensile wave, which consists with that reported by Fu *et al* [10]. In the case of reflective BC displayed in figure 4(b), compression wave reflects with an opposite propagation velocity until it meets with the ongoing piston and reflects again, which is similar to that found by Elder *et al* [6]. Accordingly, material is gathered-up gradually and the compression strengthens after each reflection with higher pressure. This case can be considered as an analogy with a dynamic wave traveling from low impedance material to high impedance (infinite impedance). As the piston driven velocity v_p decreases, which results in weaker.

Series of representative wave propagations under different compression strengths with piston velocity ranging from 0.5 to 5.0 km s^{-1} were plotted in figure 6. The material jumps from the non-shocked to the shocked state in a narrow time bandwidth nearly instantaneously with

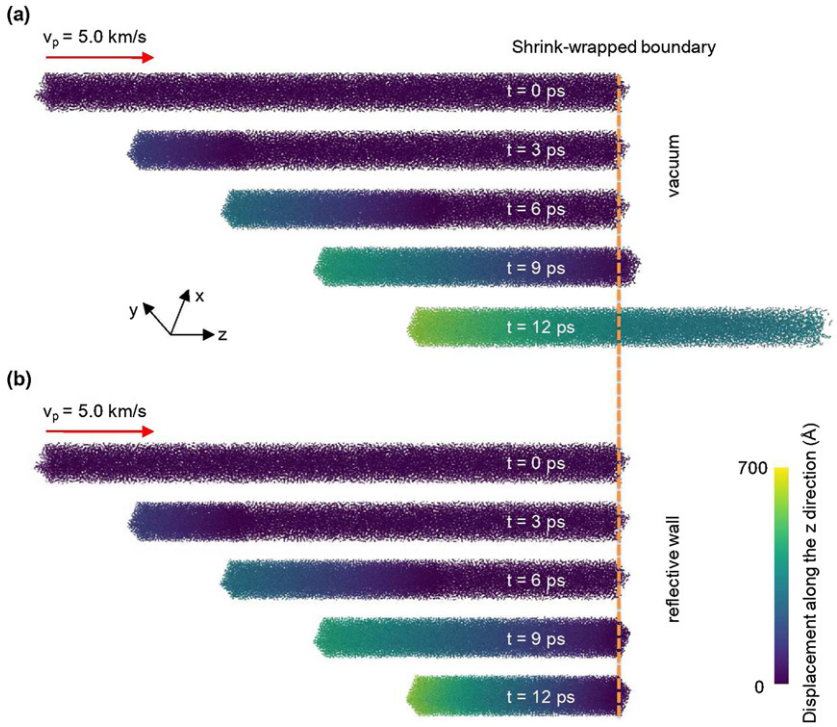

Figure 4. Temporal evolutions of particle displacement along the impact direction in APE bar at 100 K with (a) a free open-end and (b) a reflective wall at piston speed of 5.0 km s^{-1}.

an almost vertical front. A single sharp front is travelling at a constant velocity under each compression strength with different v_p. Taking a look at the shock front profile at a given point in time ($t = 5$ ps as an example) as summarized in figure 7, the thickness of shock front (denoted as t_{sf}) shrinks as compression strength enhances with larger v_p.

Contrary to the acoustic wave-induced isentropic changes, common structural deformation at the shock front under high strain rate is viscous flow in a fluid or plastic flow in a solid [10]. The compression rate in a shock wave (denoted as $\dot{\varepsilon}$) is calculated as the ratio of v_p to t_{sf} [34]. Accordingly, the power law relationship between $\dot{\varepsilon}$ and P_{zz} was provided in figure 8 with an exponent of 1.069 ± 0.002. Similar results were reported in the previous works, such as polyethylene glycol diacrylate (PEGDA) hydrogels and glycerol with power-law exponent of 1.4 [34] and of 2.1 [35], respectively. Luo *et al* [34] mentioned that a value between 1 and 2 is also observed in granular and laminated composites [36] experimentally. These existing results provide evidence to prove the rationality of our results.

The variation of t_{sf} with respect to P_{zz} was illustrated in figure 9. t_{sf} is proportional to the power exponential function of P_{zz} with an exponent of -0.427 ± 0.003, where the exponent represents the deformation mechanism [34]. A close value as -0.65 was obtained in the study on PEGDA [34]. The obtained relationship in the current study quantitatively demonstrates that the thickness of shock front shrinks as the hydrodynamic pressure increases, which has been qualitatively mentioned in figure 7. As the absolute value of the exponent increases, a steeper shock front resulting from the enhanced hydrodynamic pressure accelerates the

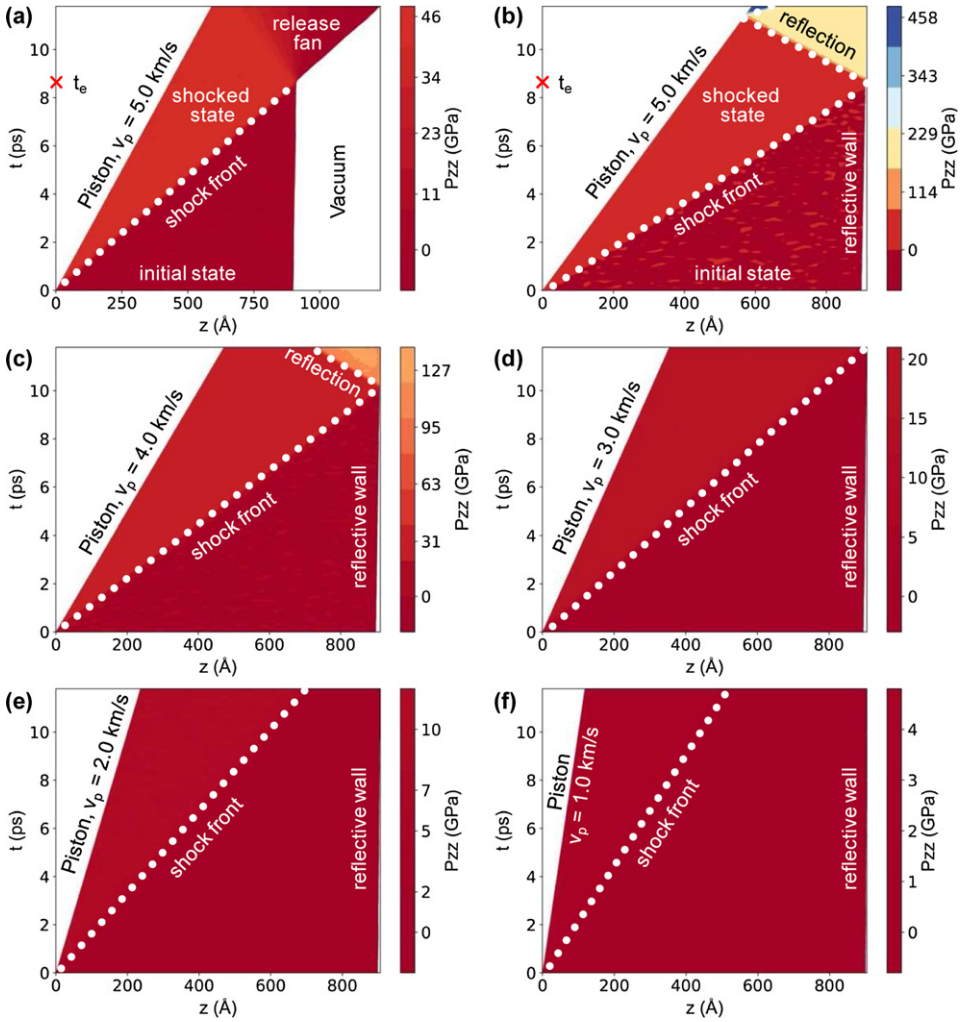

Figure 5. Position-time ($z - t$) diagrams of pressure parallel to the shock P_{zz} for a shock with piston velocity of (a) 5.0 km s^{-1} with a free open-end, (b) 5.0 km s^{-1} with a reflective wall, (c) 4.0 km s^{-1} with a reflective wall, (d) 3.0 km s^{-1} with a reflective wall, (e) 2.0 km s^{-1} with a reflective wall and (f) 1.0 km s^{-1} with a reflective wall. Each shock front is labeled with white dots. These results are for one representative replica configuration at 100 K. compression strength, the wave front moves slower as described in (c)–(f).

plastic deformation [37]. Inferred from these results, strong and positive correlations between v_p and v_s (P_{zz}) were concluded according to the descriptions in figures 5–9. The quantitative relationships will be addressed in the next section.

3.2. Hugoniot relations

Shock Hugoniot, as the set of thermodynamic states transformed from a given initial state to those after the shock front passes, is a common way to characterize the shock response of a material [6]. On the basis of the mass, momentum, and energy conservations in the shock wave

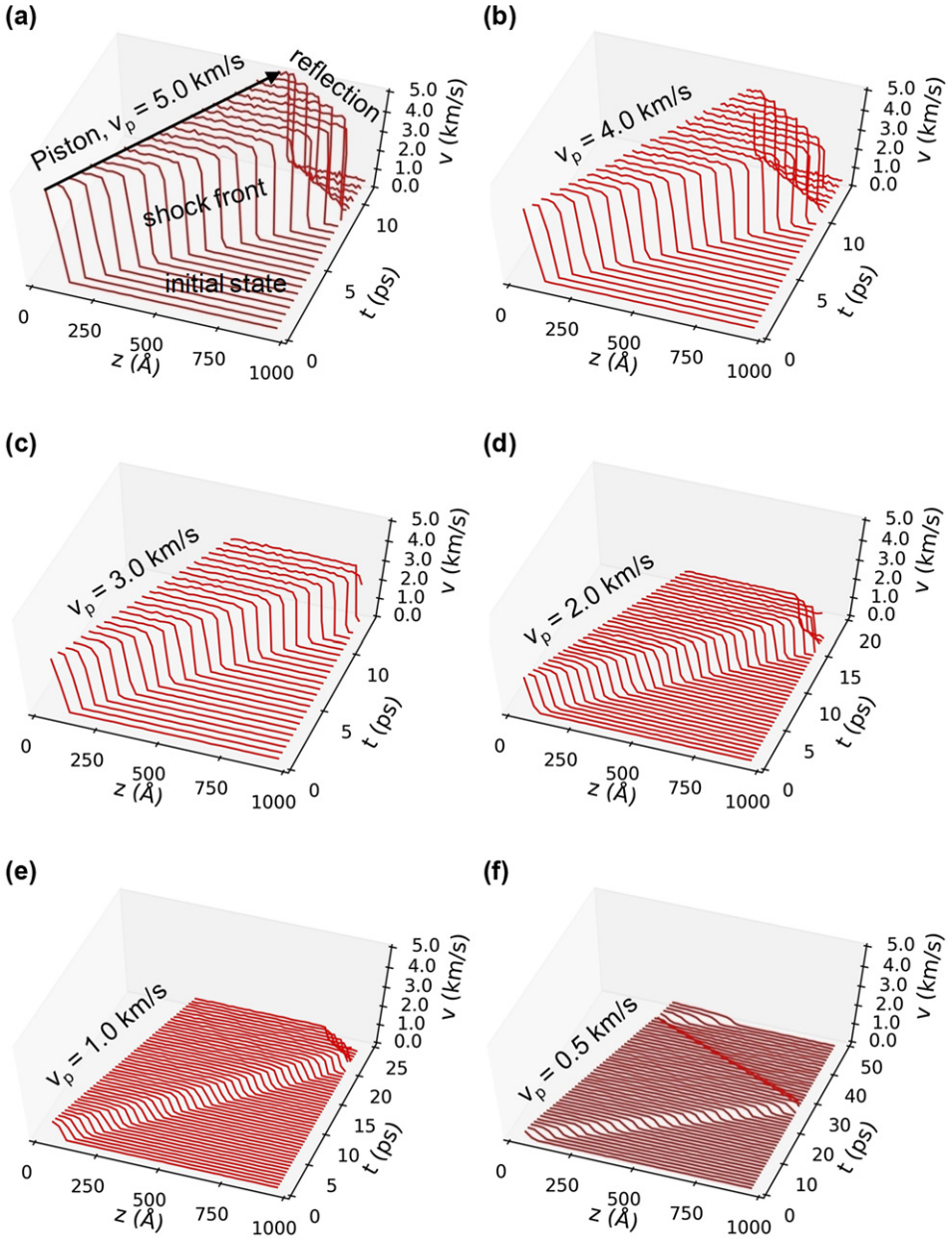

Figure 6. NEMD-computed moving compression wave profile for (a) $v_p = 5.0$ km s^{-1}, (b) $v_p = 4.0$ km s^{-1}, (c) $v_p = 3.0$ km s^{-1}, (d) $v_p = 2.0$ km s^{-1}, (e) $v_p = 1.0$ km s^{-1} and (f) $v_p = 0.5$ km s^{-1} displaying a single sharp front with reflective BC. These results are for one representative replica configuration at 100 K.

system, three important Hugoniot relations such as shock velocity–particle velocity (v_s–v_p), hydrodynamic pressure–particle velocity (P–v_p), and hydrodynamic pressure–normalized volume (P–V/V_0) can be established as the independent equations to solve the Rankine–Hugoniot

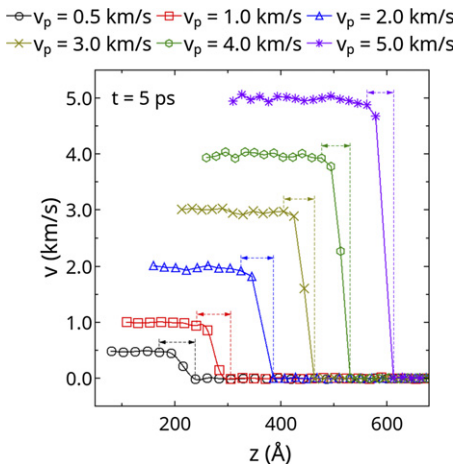

Figure 7. NEMD-computed distribution of particle velocity along the compression direction at given time ($t = 5$ ps) with different shock strengths. Shock front thickness (width of jump region in each shock profile) varies with respect to v_p. These results are for one representative replica configuration at 100 K.

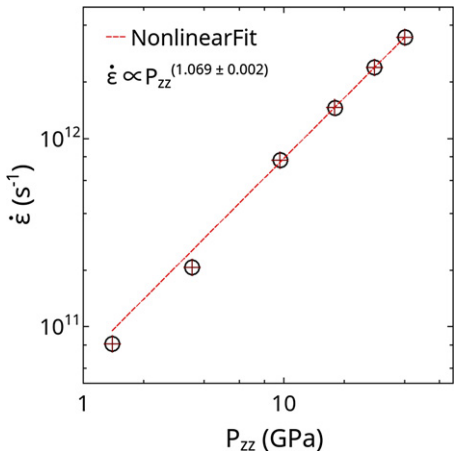

Figure 8. Relationship between the rate of compression $\dot{\varepsilon}$ and the hydrodynamic pressure P_{zz} computed by NEMD at 100 K.

jump equations [38, 39]. The subscript '0' of variables refers to the quantity in the initial un-shocked reference state at each target temperature.

For many materials, the v_s–v_p Hugoniot relation can be simplified into a linear function as,

$$v_s = C_0 + Sv_p, \tag{1}$$

where C_0 and S are the bulk sound speed and a constant relevant to the material, respectively. However, owing to that polymer behaves in a nonlinear fashion [39], the Hugoniot in shock

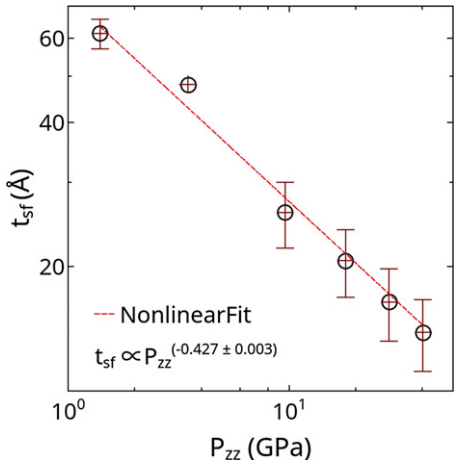

Figure 9. Relationship between the thickness of shock front t_{sf} and the hydrodynamic pressure P_{zz} computed by NEMD at 100 K.

velocity–particle velocity space is given by a quadratic polynomial function.

$$v_s = C_0 + Sv_p + Rv_p^2, \tag{2}$$

where R is another constant of the material determined by experiments with the unit of s km^{-1}.

The equation of momentum conservation is expressed as,

$$P - P_0 = \rho_0 v_s v_p. \tag{3}$$

Putting equation (2) into equation (3), considering the virial stress (denoted as P_{zz}) paralleled to the shock direction (z-direction) and initial zero pressure, the above expression can be rewritten as following, which is useful in studying shock wave interaction.

$$P_{zz} = \rho_0(C_0 + Sv_p + Rv_p^2)v_p. \tag{4}$$

According to the mass conservation,

$$\frac{\rho}{\rho_0} = \frac{v_s - v_0}{v_s - v_p} = \frac{V_0}{V} \tag{5}$$

the following relation can be obtained.

$$v_p = v_s\left(1 - \frac{V}{V_0}\right). \tag{6}$$

Putting equation (2) into equation (6), substituting equation (6) first and then back substituting into equation (4), the Hugoniot in the P–V/V_0 plane can be described as

$$P_{zz} = \frac{\rho_0\left\{\left[S\left(1-\frac{V}{V_0}\right)-1\right]^2 - 2C_0R\left(1-\frac{V}{V_0}\right)^2 + \left[S\left(1-\frac{V}{V_0}\right)-1\right]\sqrt{\left[S\left(1-\frac{V}{V_0}\right)-1\right]^2 - 4C_0R\left(1-\frac{V}{V_0}\right)^2}\right\}}{2R^2\left(1-\frac{V}{V_0}\right)^3}. \tag{7}$$

Table 1. Predicted material parameters of glassy APE at 100 K.

Parameter	Fitting function	Computational method	
		NEMD	MSST
C_0 (km s^{-1})	Equation (2) (v_s–v_p relation)	2.610 ± 0.007	2.720 ± 0.015
	Equation (4) (P_{zz}–v_p relation)	2.326 ± 0.016	2.758 ± 0.035
	Equation (7) (P_{zz}–V/V_0 relation)	\	2.700 ± 0.055
S	Equation (2) (v_s–v_p relation)	1.709 ± 0.006	1.636 ± 0.021
	Equation (4) (P_{zz}–v_p relation)	1.597 ± 0.009	1.667 ± 0.045
	Equation (7) (P_{zz}–V/V_0 relation)	\	1.641 ± 0.033
R (s km^{-1})	Equation (2) (v_s–v_p relation)	-0.022 ± 0.001	-0.013 ± 0.001
	Equation (4) (P_{zz}–v_p relation)	-0.056 ± 0.001	-0.012 ± 0.001
	Equation (7) (P_{zz}–V/V_0 relation)	\	-0.014 ± 0.002

The Hugoniot illustrates as a collection of finale shock states rather than the path of the Hugoniot continuously from the initial state.

Referring to the dynamic wave propagation driven by different piston velocities illustrated in figure 6, the average value of the last 2000 steps in 20 ps simulation period for each variable of interest was monitored in MSST calculations, which were at equilibrated state behind the shock. Both NEMD- and MSST-computed scatters shown in figures 10(a) and (b) indicate that when the piston is driven faster, that is, particle moves quickly, the induced shock wave travels more rapidly accompanied by higher pressure. A quadratic relation between v_s and v_p, and a positive correlation nonlinearly P_{zz} and v_p were quantified by the equations (2) and (4), respectively. The values of bulk sound speed C_0 with km s^{-1} unit, dimensionless constant S and another material constant R at $T_0 = 100$ K were listed in table 1. The current results agree well with the experimental measurements on the shocked PE with average density 0.916 g cm^{-3} [40] (blue dot line). Taking much higher computational efficiency and better self-consistency in prediction into account, MSST method is more convenient and appropriate to examine the temperature dependence of Hugoniot behaviors in the following.

As illustrated in figures 10(d)–(f), a high temperature reduces the bulk sound speed C_0 of APE. Asay *et al* [41] examined the temperature dependence of the acoustic velocities in PMMA experimentally. Monotonically decreasing relationship between sound speed and temperature was reported. In addition, Zaretsky and Kanel [42] further discussed the response of PMMA to shock-wave loading at elevated temperatures. The measurements of Hugoniots of PMMA demonstrate that the sound speed increases as the temperature decreases. Hence, the temperature dependence of sound speed obtained here is consistence with the existing experimental measurements [41, 42]. In addition, the inverse variation with respect to the temperature of the material constant S was observed, which indicates that the material is easier to compress at higher temperature. The similar trend of the absolute value of R was also obtained. Cross over the T_g range, an obvious rise of S ($|R|$) was visible following by a slowdown even to be flatten out. It can be assumed that the temperature-sensitivity of the compressibility in APE weakens during the transition from glassy state to rubbery state.

The data marked as blue square '□' was calculated by NEMD at 200 K of APE in literature [10]. In addition, the data marked as red horizontal line '–' and violet diagonal cross '×' was obtained by MSST and density functional theory (DFT) at ambient temperature of APE [43], respectively. Locating near the data points obtained by NEMD, MSST and DFT in the existing works, the present results are acceptable with close values. It should be pointed out

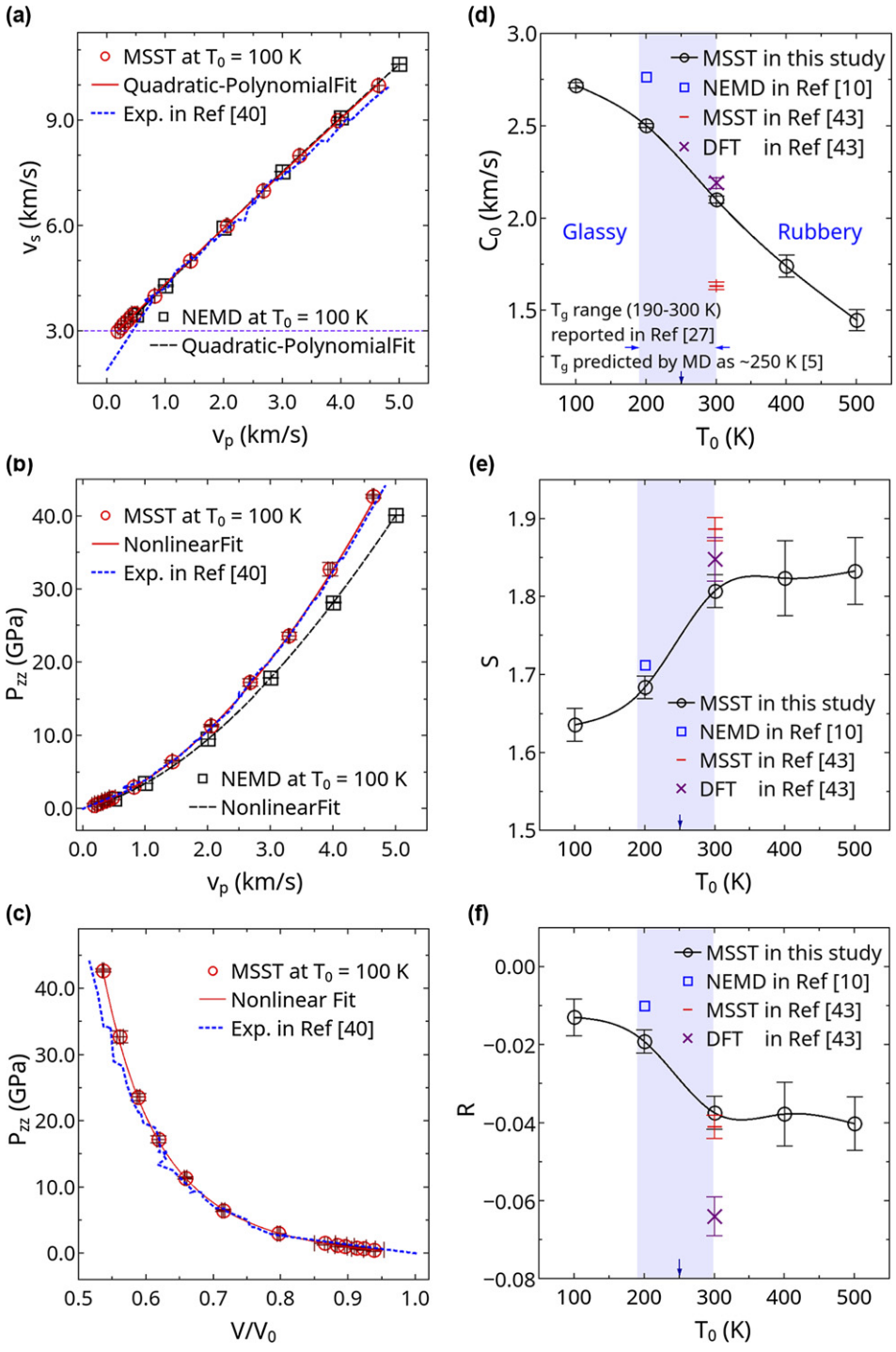

Figure 10. Hugoniot relations of (a) v_s–v_p, (b) P_{zz}–v_p, (c) P_{zz}–V/V_0, and variations of constants (d) C_0, (e) S, (f) R of APE with respect to the temperature.

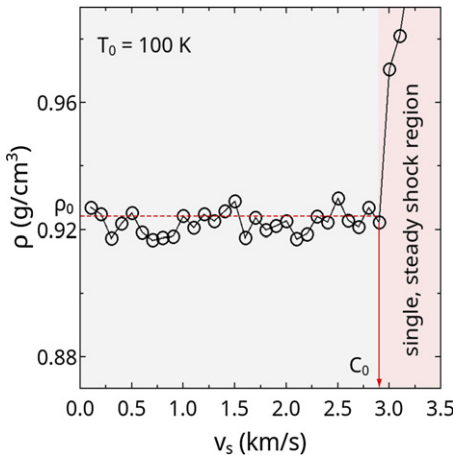

Figure 11. Variation of density with respect to shock velocity taking one representative replica configuration at $T_0 = 100$ K as an example to find the critical shock velocity for steady shock.

that the above values slightly deviate from those measured experimentally focused on semi-crystalline PE as $C_0 = 2.86\,\mathrm{km\,s^{-1}}$, $S = 1.57$ [44] and $C_0 = 2.51\,\mathrm{km\,s^{-1}}$, $S = 1.97$ [45] at room temperature with higher density at equilibrium. The similar difference due to the influence of morphologies was also supported by the works carried out by Fan *et al* [3] and Fröhlich *et al* [46], which pointed out that the computational results by MD are lower than those obtained in experiments.

3.3. Stability of dynamic wave

The dynamic compression may cause shock waves or quasi-isentropic waves. Correspondingly, the material is compressed to thermodynamic states on the shock Hugoniot or lying between the isentrope and the shock Hugoniot, respectively [33]. Based on the fact that only steady shock waves can be simulated to constrain the shock-propagation-direction stress to the Rayleigh line and energy to the Hugoniot energy condition, MSST can be taken as an approach to determine the critical shock velocity for generating a steady shock wave.

As illustrated in figure 11, a density jump was observed after a period of slight oscillation near the equilibrated density ρ_0 (marked as a red dash line) without shock compression. The shock velocity v_s induced the sharp transition of the density was recorded as the critical shock velocity. A single, steady shock wave can be generated by a shock compression with a speed greater than the critical shock velocity. On the contrary, a dynamic compression with velocity lower than the critical shock velocity may generate multi-wave propagating at a non-constant speed and taking the material to thermodynamic states deviating from the shock Hugoniot. Mathematically, the intercept in v_s–v_p relation is the bulk sound speed C_0 as described in figure 10(a). Obviously, the critical shock velocity equals to C_0. The discontinuity shock in density at C_0 is due to $\partial^2 P_{zz}/\partial V^2 < 0$ around the initial pressure [33], resulting in that no straight Rayleigh lines can be accessible in a region. Across the region without single shocks, straight Rayleigh lines can be captured in MSST and single, stable shocks occur.

The critical shock velocity, that is, the bulk sound speed C_0 is inversely correlated with the target temperature T_0 as illustrated in figure 10(d). In other words, a larger C_0 is one of the

intrinsic properties of a system with a higher density at equilibrium. Travelling faster than the predicted bulk sound speed at a given temperature, a shock wave propagates steadily. Looking back to the model settings mentioned in sections 3.1 and 3.2, the minimum value of v_s was chosen as 3.0 km s^{-1} (an example can be referred to the violet dash line marked in figure 10(a)), which guarantee the generation of stable shock waves. Correspondingly, sharp shock fronts are clearly to be observed in figures 5–7.

As displayed in figures 5 and 6, a single plastic wave propagates through the APE bar in each case, whose response is considered as over-driven with a planar shock (as illustrated in figures 6 and 7) resulting in a steep gradient in all thermodynamic properties. The Hugoniot elastic limit can potentially be zero for amorphous materials [33]. A faster elastic precursor shock ahead a primary plastic wave front in APE was not observed even when the shock strength decreases.

3.4. Discussion

Shock propagation speed should be greater than bulk sound speed, which is the intercept in v_s–v_p relation. If the shock velocity is less than the bulk sound speed, no compression occurs in MSST calculation. A piecewise change wave was observed as the result of the piston induced shock velocity less than the bulk sound speed in existing NEMD computations on amorphous carbon [33]. Different from the steep front travelling at a constant velocity illustrated in figures 6 and 7, only the leading edge of the unsteady wave propagates at the bulk sound speed. In other words, adopting the propagation velocity of the unsteady wave as the shock velocity will result in an underestimation.

The critical steady shock velocity was determined by the density jump of the system that a compressive wave passing over as demonstrated in figure 11. Higher than the predicted critical value, a single and steady shock wave can be identified easily with a steep front and a constant propagation velocity. And then, the related results obtained by both NEMD and MSST should be have a good agreement. Otherwise, quasi-isentropic waves with propagation velocity less than the bulk sound speed, compress the material along the path that describes continuity rather than a jump by Hugoniot.

A shock travels steadily at a velocity greater than the critical value, resulting in over-driven the APE with plastic deformation. This is equivalent to that the initial reference state coincide with the final reference state explained by the continuous Hugoniot method [2].

4. Conclusions

From the Eulerian viewpoint, e.g. NEMD computations, an increase in the particle velocity and pressure of APE bar ahead of the piston was observed as the result of the piston compression, which causes a shock wave to travel forward at velocity v_s in space as illustrated in figures 4–7. Only a single plastic wave was observed propagating at a constant velocity in APE as visualized in figures 5 and 6. On the other hand, following a Langrangian point, e.g. MSST calculations, the responses of the material at shock equilibrated state, such as density, pressure and particle velocity as shown in figures 10 and 11, can be described to restrain the system to the shock Hugoniot and the Rayleigh line.

As the piston moves fast, the induced shock travels at a faster velocity with a higher pressure. Accompanied by the piston driven enhancement, the shock front shrinks into nearly a planar one. An exponential relation with an exponent greater than 1 between the compression rate and the hydrodynamic pressure was fitted. On the other hand, the thickness of shock front varies with respect to the hydrodynamic pressure in an exponential relation with a negative power.

Accordingly, shock pressure dependence of the thickness of shock front was described quantitatively. Hugoniot relations, as particle velocity–shock velocity (v_s–v_p), hydrodynamic pressure–particle velocity (P_{zz}–v_p) and hydrodynamic pressure–normalized volume (P_{zz}–V/V_0), were presented to examine the shock wave interactions. The bulk sound speed and material constants characterizing compressibility were predicted with reliable values compared with the existing results. Temperature-dependency was clarified as that high temperature reduces the bulk sound speed with low density and improves the compressibility of material. The temperature-sensitivity of compressibility weakens or even disappears during the transition from glassy state to rubbery state.

The critical shock velocity, as the bulk sound speed at given temperature, was predicted to guarantee the stable shock wave propagation in APE. Only plastic shock wave travelling at a constant velocity greater than the bulk sound speed generates in APE resulting in the over-driven in the material.

The characterization presented in this paper could provide useful tools to depict the wave propagation and interaction, which is helpful to determine the controlling parameters and provide design guidelines for further and deeper research.

Acknowledgment

This work was funded by the National Natural Science Foundation of China grant 11672314. The computations were supported by National Supercomputing Center in Shenzhen (Shenzhen Cloud Computing Center) and the Computing Facility, Institute of Mechanics, Chinese Academy of Sciences. The authors declare that there is no conflict of interest regarding the publication of this article.

ORCID iDs

Lijuan Liao https://orcid.org/0000-0003-1753-6373

References

[1] Pocius A V 2012 *Adhesion and Adhesives Technology* (Munich: Carl Hanser Verlag) pp 1–16
[2] Lane J M D and Marder M P 2006 Molecular dynamics of shock fronts and their transitions in Lennard–Jonesium and tin arXiv:cond-mat/0607335
[3] Xie F, Lu Z, Yang Z, Hu W and Yuan Z 2016 Mechanical behaviors and molecular deformation mechanisms of polymers under high speed shock compression: a molecular dynamics simulation study *Polymer* **98** 294–304
[4] Fu Y and Song J-H 2015 Heat flux expressions that satisfy the conservation laws in atomistic system involving multibody potentials *J. Comput. Phys.* **294** 191–207
[5] Meng C, Liao L and Huang C 2018 Study on failure mechanism of Cu-polyethylene-Cu sandwich structure by molecular dynamics simulation *Comput. Mater. Sci.* **154** 315–24
[6] Elder R M, O'Connor T C, Chantawansri T L, Sliozberg Y R, Sirk T W, Yeh I C, Robbins M O and Andzelm J W 2017 Shock-wave propagation and reflection in semicrystalline polyethylene: a molecular-level investigation *Phys. Rev. Mater.* **1** 1–17
[7] He L, Sewell T D and Thompson D L 2011 Molecular dynamics simulations of shock waves in oriented nitromethane single crystals *J. Chem. Phys.* **134** 124506
[8] Min S H and Berkowitz M L 2018 A comparative computational study of coarse-grained and all-atom water models in shock Hugoniot states *J. Chem. Phys.* **148** 144504

[9] He L, Wang F, Zeng X, Yang X and Qi Z 2020 Atomic insights into shock-induced spallation of single-crystal aluminum through molecular dynamics modeling *Mech. Mater.* **143** 103343
[10] Fu Y, Michopoulos J and Song J-H 2015 Dynamics response of polyethylene polymer nanocomposites to shock wave loading *J. Polym. Sci.* B **53** 1292–302
[11] Connor T C O, Elder R M, Sliozberg Y R, Sirk T W, Andzelm J W and Robbins M O 2018 Molecular origins of anisotropic shock propagation in crystalline and amorphous polyethylene *Phys. Rev. Mater.* **2** 035601
[12] Reed E J, Fried L E and Joannopoulos J D 2003 A method for tractable dynamical studies of single and double shock compression *Phys. Rev. Lett.* **90** 235503
[13] Schmitt R G, Thompson A P and Aidun J B 2010 Enabling R & D for accurate simulation of non-ideal explosives *Sandia Report, SAND2010-6831, Sandia National Laboratory, Albuquerque, New Mexico*
[14] Chen J, Chen W, Chen S, Zhou G and Zhang T 2020 Shock Hugoniot and Mie-Grüneisen EOS of TiAl alloy: a molecular dynamics approach *Comput. Mater. Sci.* **174** 109495
[15] Neogi A and Mitra N 2017 Shock induced deformation response of single crystal copper: effect of crystallographic orientation *Comput. Mater. Sci.* **135** 141–51
[16] Neogi A and Mitra N 2017 A metastable phase of shocked bulk single crystal copper: an atomistic simulation study *Sci. Rep.* **7** 1–11
[17] Neogi A and Mitra N 2016 Shock compression of polyvinyl chloride *J. Appl. Phys.* **119** 165903
[18] Neogi A and Mitra N 2016 Shock induced phase transition of water: molecular dynamics investigation *Phys. Fluids* **28** 027104
[19] Shan T-R, Wixom R R, Mattsson A E and Thompson A P 2013 Atomistic simulation of orientation dependence in shock-induced initiation of pentaerythritol tetranitrate *J. Phys. Chem.* B **117** 928–36
[20] Reed E J, Riad Manaa M, Fried L E, Glaesemann K R and Joannopoulos J D 2008 A transient semimetallic layer in detonating nitromethane *Nat. Phys.* **4** 72–6
[21] Reed E J, Fried L E, Henshaw W D and Tarver C M 2006 Analysis of simulation technique for steady shock waves in materials with analytical equations of state *Phys. Rev.* E **74** 1–9
[22] Fu Y, Michopoulos J and Song J-H 2015 Coarse-grained molecular dynamics simulations of epoxy resin during the curing process *Comput. Mater. Sci.* **107** 24–32
[23] Fu Y and Song J-H 2015 Large deformation mechanism of glassy polyethylene polymer nanocomposites: coarse grain molecular dynamics study *Comput. Mater. Sci.* **96** 485–94
[24] Hossain D, Tschopp M A, Ward D K, Bouvard J L, Wang P and Horstemeyer M F 2010 Molecular dynamics simulations of deformation mechanisms of amorphous polyethylene *Polymer* **51** 6071–83
[25] Martínez L, Andrade R, Birgin E G and Martínez J M 2009 PACKMOL: a package for building initial configurations for molecular dynamics simulations *J. Comput. Chem.* **30** 2157–64
[26] Auhl R, Everaers R, Grest G S, Kremer K and Plimpton S J 2003 Equilibration of long chain polymer melts in computer simulations *J. Chem. Phys.* **119** 12718–28
[27] Nikkhah S J, Moghbeli M R and Hashemianzadeh S M 2016 Dynamic study of deformation and adhesion of an amorphous polyethylene/graphene interface: a simulation study *Macromol. Theory Simul.* **25** 533–49
[28] Plimpton S 1995 Fast parallel algorithms for short-range molecular dynamics *J. Comput. Phys.* **117** 1–19
[29] Stukowski A 2009 Visualization and analysis of atomistic simulation data with OVITO–the open visualization tool *Modelling Simul. Mater. Sci. Eng.* **18** 015012
[30] Yi P and Rutledge G C 2011 Molecular simulation of bundle-like crystal nucleation from *n*-eicosane melts *J. Chem. Phys.* **135** 0 24903
[31] Yankova T S, Bobrovsky A Y and Vorobiev A K 2012 Order parameters ⟨p2⟩, ⟨p4⟩, and ⟨p6⟩ of aligned nematic liquid-crystalline polymer as determined by numerical simulation of electron paramagnetic resonance spectra *J. Phys. Chem.* B **116** 6010–6
[32] Islam M M, Cherukara M, Antillon E and Strachan A 2019 Shock-induced chemistry: molecular dynamics and coarse grain modeling *Computational Approaches for Chemistry Under Extreme Conditions* ed B C Barnes, J K Brennan, E F C Byrd, S Izvekov, J P Larentzos and B M Rice vol 28 (Berlin: Springer) pp 229–82
[33] Reed E J, Maiti A and Fried L E 2010 Anomalous sound propagation and slow kinetics in dynamically compressed amorphous carbon *Phys. Rev.* E **81** 1–9

[34] Luo K, Yudewitz N, Subhash G and Spearot D E 2019 Effect of water concentration on the shock response of polyethylene glycol diacrylate (PEGDA) hydrogels: a molecular dynamics study *J. Mech. Behav. Biomed. Mater.* **90** 30–9
[35] Kanel' G I, Savinykh A S, Garkushin G V and Razorenov S V 2017 Evaluation of glycerol viscosity through the width of a weak shock wave *High Temp.* **55** 365–9
[36] Zhuang S, Ravichandran G and Grady D E 2003 An experimental investigation of shock wave propagation in periodically layered composites *J. Mech. Phys. Solids* **51** 245–65
[37] Meyers M A 1994 *Dynamic Behavior of Materials* (New York: Wiley)
[38] Zhang Z 2016 *Shock Waves, Rock Fracture and Blasting: Theory and Application* (Oxford: Butterworth-Heinemann) pp 39–66
[39] Hazell P J 2016 Shock loading of polymer composites dynamic deformation, damage and fracture in composite materials and structures *Damage and Fracture in Composite Materials and Structures* ed V V Silberschmidt (Cambridge: Woodhead publishing) pp 337–63
[40] Mader C L, Gibbs T R, Hopson J W, Marsh S P, Hoyt M S, Thayer K V, Craig B G and Deal W E 1980 *LASL Shock Hugoniot Data* ed S P Marsh (Berkeley, CA: University of California Press)
[41] Asay J R, Lamberson D L and Guenther A H 1969 Pressure and temperature dependence of the acoustic velocities in polymethylmethacrylate *J. Appl. Phys.* **40** 1768–83
[42] Zaretsky E B and Kanel G I 2019 Response of poly(methyl methacrylate) to shock-wave loading at elevated temperatures *J. Appl. Phys.* **126** 085902
[43] Chantawansri T L, Sirk T W, Byrd E F C, Andzelm J W and Rice B M 2012 Shock Hugoniot calculations of polymers using quantum mechanics and molecular dynamics *J. Chem. Phys.* **137** 204901
[44] Bourne N K 2016 On the shock response of polymers to extreme loading *J. Dyn. Behav. Mater.* **2** 33–42
[45] Bourne N K and Millett J C F 2008 Tacticity in shocked polymer hydrocarbons *J. Mater. Sci.* **43** 185–9
[46] Fröhlich M G, Sewell T D and Thompson D L 2014 Molecular dynamics simulations of shock waves in hydroxyl-terminated polybutadiene melts: mechanical and structural responses *J. Chem. Phys.* **140** 02490 2